Spacer and Anchor Effects on the Electronic Coupling in Ruthenium-bis-Terpyridine Dye-Sensitized TiO₂ Nanocrystals Studied by DFT

Maria J. Lundqvist,* Mattias Nilsing, and Sten Lunell

Department of Quantum Chemistry, Uppsala University, Box 518, S-751 20 Uppsala, Sweden

Björn Åkermark

Department of Organic Chemistry, Stockholm University, S-106 91 Stockholm, Sweden

Petter Persson

Department of Chemical Physics, Lund University, Box 124, S-221 00 Lund, Sweden

Received: June 28, 2006; In Final Form: August 4, 2006

Structural and electronic properties of TiO₂ nanoparticles sensitized with a set of Ru^{II}(tpy)₂ based dyes have been investigated using density functional theory (DFT) calculations combined with time-dependent (TD) DFT calculations. The effects of carboxylic and phosphonic acid anchor groups, as well as a phenylene spacer group, on the optical properties of the dyes and the electronic interactions in the dye-sensitized TiO₂ nanoparticles have been investigated. Inclusion of explicit counterions in the modeling shows that the description of the environment is important in order to obtain a realistic interfacial energy level alignment. A comparison of calculated electronic coupling strengths suggests that both the nature of the anchor group and the inclusion of the phenylene spacer group are capable of significantly influencing electron-transfer rates across the dye−metal oxide interface.

1. Introduction

Dye-sensitized nanostructured TiO₂ electrodes can accomplish photoinduced charge separation in which photoexcitation of appropriate dye molecules under favorable conditions can cause extremely efficient interfacial electron injection from the dye into the TiO₂ conduction band.[1−3] The charge separation can be used, e.g., for environment-friendly renewable solar energy conversion in so-called dye-sensitized solar cells (DSSCs)[4] as well as to drive further redox reactions, e.g., with the ambition to perform artificial photosynthesis[5] or to cause photocatalytic degradation of, e.g., pollutants.[6]

Ruthenium polypyridyl complexes have been extensively studied as photosensitizers in solar energy conversion applications. Among the most widely studied complexes are Ru^{II}(bpy)₃ (bpy = 2,2′-bipyridine) derivatives, such as the so-called N3 dye, due to their favorable excited-state properties. Complexes based on the 2,2′:6′,2′′-terpyridine (tpy) ligand are attractive alternatives because they offer the possibility of forming linear dye complex structures via substitution at the 4′-position of the central pyridyl in each tpy ligand. The excited-state lifetime for Ru^{II}(tpy)₂ is generally much shorter than for Ru^{II}(bpy)₃ and N3 (∼250 ps[7] for Ru^{II}(tpy)₂ compared with ∼1 μs lifetime of Ru^{II}(bpy)₃[8]), but nonetheless the excited Ru^{II}(tpy)₂ chromophore is known to efficiently inject electrons into TiO₂.[9] In response to the wide interest in ruthenium dyes from both a fundamental and a technological perspective, a large number of quantum chemical studies of ruthenium dyes have also been published in recent years, see for instance, refs 10−24.

The dyes most commonly used in photoelectrochemical applications are anchored to the metal oxide via carboxylic acid groups that bind to the surface. Phosphonic acid is an alternative to the carboxylic acid that typically binds more strongly to the surface.[25,26] Stronger adsorption of the phosphonic acid must, however, be balanced against the fact that it may weaken the interfacial electronic coupling in such a way as to slow the interfacial electron injection.[27] In addition, so-called spacer groups can be introduced between the chromophore and the anchor group in order to spatially separate the chromophore and semiconductor and to control the electronic interactions between the dye and the nanoparticle.[28−30] Rigid spacers are, in this context, of particular interest, as they provide the possibility to tune the electronic properties with full control over the distance dependence of the surface electron transfer (ET).[31,32]

Computer simulations are now applicable to increasingly realistic model systems, providing information that can help to understand and optimize both the structure and the electronic properties of dye−TiO₂ interfaces and thus complement experimental work.[33] The size and complexity of these nanosized heterogeneous systems impose significant computational challenges in both the choice of methods and chemical models.[33] A common computational approach is to perform calculations of adsorbate−nanocrystal surface systems using periodic boundary conditions. With a relatively small two-dimensional periodic TiO₂ slab model, the electronic structure of TiO₂ can be well described and a density of states (DOS) with a band gap close to the bulk value can be obtained.[34] However, large dye molecules, such as Ru^{II}(tpy)₂, require the use of very large unit cells in order to avoid undesirable interactions between dye molecules across the periodic cell boundaries. Such calculations

* Corresponding author. E-mail: Maria.Lundqvist@kvac.uu.se. Telephone: +46−18-4715833. Fax: +46-18-4715830.

are computationally very expensive. An alternative approach to periodic calculations is to use cluster models, which enables studies of the interaction of large adsorbates with nanostructured TiO_2 substrates without introducing any adsorbate−adsorbate interactions. However, the computational cost grows quickly with increasing cluster size because every TiO_2 unit adds 38 electrons to the system. With current computational size limitations for accurate quantum chemical methods, typical cluster models will consist of a large portion of surface atoms and will therefore have a higher degree of surface reorganization than the periodic models. We have developed a set of relatively large neutral and stoichiometric TiO_2 cluster models that are bare clusters of anatase type.[35−37] Such large cluster models have also been used to investigate the interfacial properties of several dyes bound to TiO_2 nanocrystals.[30,38−40] In this paper, we use a cluster model containing 46 TiO_2 units that we have used previously to study the adsorption of phosphonic and carboxylic acid adsorbed to an anatase (101) type surface section.[37]

For photosensitization of TiO_2, the position of the excited-state energy level of the dye relative to the substrate conduction band (CB) edge is an important factor because the electron injection from the excited dye molecule to the CB of the semiconductor requires that the first excited-state energy level of the dye is higher than the edge of the CB.[4] However, the energetic position of the CB edge is not fixed, but can shift in both directions when the environment around the semiconductor is changed, for example, by adsorption of different cations on the TiO_2 surface and thus influence the injection process.[41] A second critical factor for efficient photoinduced surface ET is the interfacial electronic coupling, which can be estimated using the mixing of dye and semiconductor orbitals as a simple measure of the effective lifetime broadening according to the Newns−Anderson model[30,33,34] as long as the excited state of the dye is sufficiently high above the CB edge to be in the so-called wide-band limit.[42] In this case, the excited dye donor state is effectively in constant resonance with a quasicontinuum of substrate band acceptor states.[43] In contrast, for some systems where the excited state of the dye is situated energetically under, or very close to, the substrate CB edge, activation via nuclear motion may play a more prominent role in limiting the surface ET rate.[44] Several alternative theoretical and computational treatments of relevant surface ET processes in dye-sensitized semiconductor heterostructures have been tried in recent years.[34,45−49]

The objective of this study is to explore the effects of different anchor and spacer groups on calculated geometries, electronic structure, and spectral properties of $Ru^{II}(tpy)_2$ attached to TiO_2 nanoparticles via these groups. In particular, we investigate the interfacial electronic structure between the dyes and the TiO_2 surface in terms of molecular orbitals, effective density of states, estimated electronic coupling strengths, and injection times, as well as calculation of the lowest electronic excitations. To address the problem of level shifting of the different parts of the charged system, the effects of inclusion of explicit PF_6^- counterions are investigated on free adsorbates and sensitized systems.

2. Methods

Density functional theory (DFT) and time-dependent (TD) DFT calculations were performed in order to investigate the structural, electronic, and optical properties of a set of Ru^{II}-$(tpy)_2$ derivatives, a TiO_2 nanoparticle, and $Ru^{II}(tpy)_2$-sensitized TiO_2 nanoparticles. All calculations were performed using the Gaussian03 program.[50]
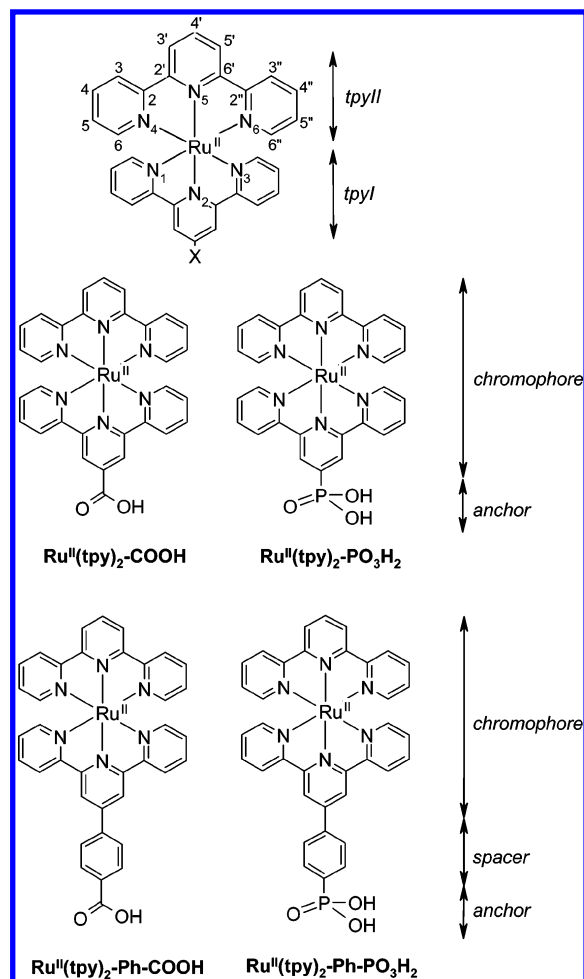

Figure 1. Investigated $Ru^{II}(tpy)_2$ derivatives and the labels used in the paper. At the top, the numbering of the pyridyl rings (N_x), the atom labeling of the tpy ligand, and the tpy ligand labels (tpyI and tpyII) in the $Ru^{II}(tpy)_2$ complex are shown.

The isolated dyes, $Ru^{II}(tpy)_2$, $Ru^{II}(tpy)_2$−COOH, $Ru^{II}(tpy)_2$−PO_3H_2, $Ru^{II}(tpy)_2$−Ph−COOH, and $Ru^{II}(tpy)_2$−Ph−PO_3H_2 (shown in Figure 1), were fully optimized using the B3LYP functional[51,52] together with the commonly used LANL2DZ effective core potentials (ECPs) and associated basis sets.[53,54] Two PF_6^- counterions were added to the geometries, and the resulting structures were then reoptimized with B3LYP/ LANL2DZ. To construct the combined $Ru^{II}(tpy)_2$-derivative−counterions systems, the $[Ru^{II}(tpy)_2][PF_6^-]_2$ crystal structure was used for guidance.[55] The ions were placed similarly to the crystal structure orientation of the PF_6^- ions with the shortest Ru−P distances (6.1−6.6 Å). To prevent the counterions from interacting with the TiO_2 surface in the sensitized system, both PF_6^- ions were placed closest to the unsubstituted tpyII ligand (see Figure 1) and one on each side of this ligand. When viewing the $Ru^{II}(tpy)_2$ moiety along the C2 symmetry axis that intersects the two 4′-tpy positions and the Ru core, the two tpy ligands form a cross. The two ions were placed in two diagonal quadrants of the cross. The whole complex, dye and ions, was then fully optimized. No symmetry constraints were imposed on any geometry optimizations. The Cartesian coordinates of the resulting optimized geometries are provided as Supporting Information.

To calculate the electronic structure and the 25 lowest singlet excitations, a combination of different ECPs and basis sets that we denote VD(T)Z was used. VD(T)Z consists of ECPs[56,57] describing the inner electrons and 31G basis sets describing the

valence electrons of O, P, N, C, and F atoms.[57] A polarization function (*d*-function), not present in the original basis set by Boutellier et al., was added to the basis set of P in order to improve its description.[27] Ruthenium was described by the LANL2DZ ECP and basis set,[53,54] and for hydrogen, the standard 6-31G basis set was used.[58] In VD(T)Z, the T in parentheses indicates an additional sp shell on O,[34,59] not present in the original basis set for oxygen that we denote VDZ. The B3LYP/VD(T)Z results were compared with the more commonly used B3LYP/LANL2DZ. The absorption spectra were convoluted as a sum of Gaussian functions using the SWizard program, revision 4.2,[60] with half-bandwidth equal to 1000 cm^{-1}.

Nanocrystalline TiO$_2$ was modeled by a large anatase cluster of 46 units, (TiO$_2$)$_{46}$, fully optimized starting from the anatase crystal structure[61] according to a previously described strategy.[35,37] The (TiO$_2$)$_{46}$ cluster is stoichiometric and charge neutral and was fully optimized with B3LYP/VDZ as a bare cluster without any saturation of dangling bonds or charge embedding applied. The ECP and basis set used for Ti (VDZ and VD(T)Z) is a 41G[62] basis set that contains a shell of sp polarization functions[63] and a large ECP describing the 18 inner electrons.[57] The ECP parameters for Ti are exponent 1.0188263 and coefficient 12.272461 (2) for the $l = 0$ projection, exponent 0.7040588 and coefficient 7.745528 (2) for the $l = 1$ projection, and the four terms for $l = 2$ have exponent 1.5920749 and the coefficients, -0.559903 (0), -7.742157 (1), 6.704284 (2), and -6.208391 (4), with the power of r in parentheses. The B3LYP/VDZ combination has been found to be an efficient computational method for TiO$_2$ nanoparticle systems.[37] An effective Ti$-$O distance distribution was obtained by a 0.1 Å artificial Gaussian broadening of the individual distances of the optimized geometry. The electronic structure as well as the lowest vertical excitations were obtained by B3LYP/VDZ and B3LYP/VD-(T)Z single point calculations on the B3LYP/VDZ optimized structure.

A composite optimization scheme was used for the geometries of the dye-sensitized nanoparticle systems. First, the carboxylic or phosphonic acids (anchors) were adsorbed in a monodentate adsorption mode on the (101) surface of the fully optimized (TiO$_2$)$_{46}$ model. The monodentate mode was used here as a prototype adsorption mode, which has been found to be a favorable mode in previous studies.[25] The anchor$-$nanoparticle systems were then fully optimized using B3LYP/VDZ. Second, the fully optimized anchor$-$nanoparticle geometries were merged with the separately B3LYP/LANL2DZ optimized substituted Ru^{II}(tpy)$_2$ dyes at the carboxylic carbon or phosphonic phosphorus atom. The orientation of the dye relative to the TiO$_2$ surface was determined by the direction of the nonbonded hydrogen of the acid, and the rotation of the dye was determined by the direction of the double-bonded oxygen of the acid functionality in the free dye. No further optimization was applied. The use of mixed computational methods for geometry optimization of the different parts were motivated by the fact that the VDZ basis set performs better for P$-$O bonds than LANL2DZ and that LANL2DZ performs better for the metal coordination sphere. The composite optimization scheme is expected to work well because the greater part of the effects of adsorption is captured by optimization of the anchor and substrate.[27,37] The electronic structure of the sensitized systems was then calculated using B3LYP and the VD(T)Z basis set as described earlier, with LANL2DZ for ruthenium. We have successfully used this method combination in previous studies.[25,27,30,33,34,40,59,64] In the analysis of the electronic structure,

an effective density of states (DOS) was constructed from the discrete one-electron molecular orbital (MO) levels through a Gaussian broadening of the individual orbital contributions by an arbitrary factor of 0.3 eV. Moreover, the five lowest excitations were calculated using TD-B3LYP/VD(T)Z for the sensitized system.

To analyze the electronic coupling strength and estimate the electron injection time between the Ru^{II}(tpy)$_2$ chromophore and the TiO$_2$ substrate, a Newns$-$Anderson approach for adsorbates on surfaces was used. The electronic coupling was estimated by how much an unoccupied adsorbate MO level change in terms of energetic shift and broadening when interacting with the substrate. In the electronic structure of the sensitized system, the adsorbate portion, p_i, of every MO, i, with orbital energy, ϵ_i, is extracted from the n basis set expansion coefficients, c_{ij}^A, centered on adsorbate atoms (A):

$$p_i = \sum_{j}^{A \in \text{ads}} (c_{ij}^A)^2 / \sum_{j}^{n} (c_{ij}^A)^2 \qquad (1)$$

The MOs that contain adsorbate portions equivalent to that of the isolated adsorbate LUMO, the LUMO (ads) levels, were identified and collected such that $\sum_i p_i \approx 1$. The center of the LUMO (ads) distribution, E_{LUMO} (ads), was then obtained by a weighted average,

$$E_{\text{LUMO}} (\text{ads}) = \sum_{i} p_i \epsilon_i \qquad (2)$$

and the adsorption induced energy shift by

$$\Delta E = E_{\text{LUMO}} (\text{ads}) - E_{\text{LUMO}} (\text{free ads}) \qquad (3)$$

where the value of E_{LUMO} (free ads) was obtained from a separate electronic structure calculation of the free adsorbate. The width of the broadening, $\hbar\Gamma$, is taken as the mean deviation of the LUMO (ads) levels

$$\hbar\Gamma = \sum_{i} p_i |\epsilon_i - E_{\text{LUMO}} (\text{ads})| \qquad (4)$$

A Lorentzian distribution, ρ, was then constructed from

$$\rho_{\text{LUMO}}(E) = \frac{1}{\pi} \frac{\left(\frac{\hbar\Gamma}{2}\right)}{(E - E_{\text{LUMO}} (\text{ads}))^2 + \left(\frac{\hbar\Gamma}{2}\right)^2} \qquad (5)$$

to display the final energy distribution of the adsorbate states.[65] The estimated electron-transfer time was obtained from the lifetime broadening through τ (fs) $= 658/\hbar\Gamma$ (meV). This approach has previously been used by our group[30,37,40] and is described in more detail in refs 30 and 37.

Molecular illustrations were made with MOLEKEL,[66] and graphs and remaining plots were made using the free software Grace-5.1.18.[67]

3. Results and Discussion

3.1. Isolated Dyes. *3.1.1. Geometry.* The geometric structure of Ru^{II}(tpy)$_2$ has been extensively studied both experimentally[55,68,69] and computationally.[18-20] The structure of Ru^{II}(tpy)$_2$ is approximately of D_{2d} symmetry. No symmetry constraints were however imposed on the calculations presented in this paper. In the calculated structure, the two tpy ligands (denoted tpyI and tpyII according to Figure 1) are planar and orthogonal

to each other. The calculated Ru−N bond distances are slightly longer than the corresponding experimental crystal structure bonds. The optimized Ru−N distances of the central pyridyls are 2.01 Å, and the remaining four bonds are 2.11 Å, compared to the crystal structure distances of 1.96−2.00 Å and 2.05−2.09 Å, respectively.[55,68,69] The overestimation of Ru−N bond lengths by the B3LYP/LANL2DZ method has previously been reported for these types of systems (see, for instance, refs 18, 17, 70, and 71). According to initial geometry optimization test calculations on $Ru^{II}(tpy)_2$, performed using B3LYP and the different basis sets, LANL2DZ or SDD[72−74] effective core potentials and associated basis set on Ru, and SDD,[75] D95V,[53] 3-21G*, or 6-31+G(d,p)[58] on the remaining atoms, showed that all basis sets slightly overestimate the Ru−N distances compared to available crystal structures.[55,68,69] However, the calculated N−Ru−N angles are highly similar to the crystal structure data.

The geometries of the isolated dyes were obtained by first a full optimization of the chromophore−(spacer)−anchor systems, followed by addition of the two counterions and then yet again a full geometry optimization. A table reporting geometry details of the optimized dyes including counterions and the corresponding individual fragments is provided as Supporting Information in Table S1.

The optimized PF_6^- ions are located at a Ru−P distance of 5.68−5.71 Å in all five dyes. In these geometries, most of the positive charge is localized at the ruthenium core (+1.24), while the negative charge is spread over the counterions (−0.85 on each PF_6), according to the Mulliken charges at the B3LYP/LANL2DZ level. The shortest counterion−tpy ligand atom distance is 2.11 Å between a fluorine atom and a tpyI hydrogen atom. In the calculations, the presence of counterions distorts the planarity of the tpy planes, similarly to what is seen in the crystal structure.[55] The twist of the pyridyl planes around the C2−C2′ and C6′−C2″ bonds, i.e., the dihedral angles N1−C2−C2′−N1′ and N1′−C6′−C2″−N1″ in both tpy ligands range from 0.2 to 1.1°, where the largest distortions are found in tpyII. The puckering of the pyridyl planes is estimated by the pyramidalization of the C2, C2′, C6′, and C2″ atoms, e.g., how much the improper torsion angle N1−C2(−C2′)−C3 deviates from planarity. The pyramidalizations are slightly larger in tpyII, 1.0−1.4°, than in tpyI, 0.0−0.9°, for all five compounds. Hence, both the measures of pyridyl twist and puckering show that the distortions from planarity are relatively small. All twist and pyramidalization values are listed in Table S2 in Supporting Information. In terms of bond length changes in the tpy framework in $Ru^{II}(tpy)_2$, the geometrical effects of the counterions are also small. The ion-induced changes in C−C and C−N bond lengths are all smaller than 0.01 Å. The maximum change in bond lengths compared to isolated Ru^{II}-$(tpy)_2$ is a Ru−N bond length change of 0.02 Å seen in $[Ru^{II}(tpy)_2−COOH][PF_6^-]_2$. The general effect on the Ru−N bonds caused by the negative ions is a slight shortening of the bonds. In unsubstituted $[Ru^{II}(tpy)_2][PF_6^-]_2$, the Ru−$N_2$ bond (tpyI) is shortened by 0.010 Å, the Ru−N_5 bond (tpyII) is elongated by 0.006 Å, and the remaining Ru−N bonds become only 0.005 and 0.006 Å shorter compared with $Ru^{II}(tpy)_2$. In the substituted dyes, this effect is somewhat more pronounced, mostly in $[Ru^{II}(tpy)_2−Ph−COOH][PF_6^-]_2$, where the Ru−$N_2$ bond becomes 0.023 Å shorter and the Ru−N_5 bond 0.010 Å longer.

The overall geometrical changes in the individual chromophore, spacer, and anchor fragments are small when connected to form the combined chromophore−spacer−anchor systems. The Ru coordination sphere, as well as the tpy ligand framework, remains almost unchanged when attaching anchor or spacer groups to the 4′-position of tpyI in $Ru^{II}(tpy)_2$. The largest bond length differences in the Ru−N, C−C, and C−N bonds are 0.01 Å. Interestingly, the attachment of an anchor group directly to the 4′-position of $Ru^{II}(tpy)_2$ affects the bond lengths in the N_2−Ru−N_5 axis by elongating the Ru−N_2 bond (tpyI) and shortening the Ru−N_5 bond (tpyII), i.e., opposite to the effect caused by the counterions. However, the effect of the counterions dominates.

In the dyes with an anchor group directly attached to tpyI, the most stable anchor orientation has the anchor double bond (C=O or P=O) close to parallel with the adjacent tpy plane. Moreover, the bond lengths within PO_3H_2, both when directly attached to the tpy ligand in $Ru^{II}(tpy)$ and when attached to the phenylene spacer, are highly similar to those of the free acid. At the B3LYP/LANL2DZ level, these bond lengths are 1.24 (C=O), 1.38 (C−O), and 0.98 Å (O−H) in the carboxylic anchor, and 1.58 (P=O), 1.70 (P−O), and 0.98 Å (O−H) in the phosphonic anchor. In the VDZ basis set, a *d*-function is present to improve the description of the phosphorus atom, and no corresponding function is present in the LANL2DZ basis set. The phosphorus−oxygen bonds in the B3LYP/VDZ optimized geometry of $Ru^{II}(tpy)_2−Ph−PO_3H_2$ are significantly shorter than the corresponding B3LYP/LANL2DZ bond lengths, and closer to those of the phosphonate group in the crystal structure of, for instance, $Ru(tpy−PO_3H_2)(2,2′-bipyridine)$-NCS.[76] The P=O and P−O bond lengths are 1.58 and 1.70 Å with LANL2DZ, 1.49 and 1.62 Å with VDZ, and 1.46 and 1.56 Å in the crystal structure. Therefore, the VDZ basis set is used to describe the anchor groups in the geometry optimization of $HPO_3H_2−(TiO_2)_{46}$ and $HCOOH−(TiO_2)_{46}$ discussed in Section 3.3. In both phenylene-containing derivatives, the phenyl plane is twisted ca. 30° out of the connecting tpy plane: 32−34° in $Ru^{II}(tpy)_2−Ph−COOH$ and 33−35° in $Ru^{II}(tpy)_2−Ph−PO_3H_2$. These results are in agreement with previous computational findings for tpy−Ph-containing systems.[18,20,77] In $Ru^{II}(tpy)_2−Ph−COOH$, the anchor C=O is close to parallel with the phenyl plane (dihedral angle 0.2°). However, in $Ru^{II}(tpy)_2−Ph−PO_3H_2$, the P=O is twisted 4 and 10° out of the phenyl plane, in the optimized geometries with and without counterions, respectively.

3.1.2. Electronic Structure: Molecular Orbitals. Absorption of visible light, i.e., electronic excitations at 400−700 nm, is of great importance for $Ru^{II}(tpy)_2$ in its role as a photosensitizer. In this region, metal-to-ligand charge transfer (MLCT) transitions are known to occur from the highest occupied molecular orbitals (HOMOs) to the lowest unoccupied molecular orbitals (LUMOs).[78] The main character of the important MOs in the highest occupied−lowest unoccupied region is listed in Table 1. The main character of the MOs for the five dyes excluding explicit counterions are listed in Table S3 in Supporting Information. In unsubstituted $Ru^{II}(tpy)_2$, the three HOMOs are of Ru d-orbital character and the main character of the LUMOs is ligand tpy−π*. Experimental evidence has shown that the primary photoexcitation in the visible region occurs from the ground state to a singlet MLCT state, ^{1}MLCT, which is a state that results from the transfer of one of the Ru d-electrons to an unoccupied tpy−π* MO mainly localized on the ligands.[78] When connected to TiO_2, fast electron injection (femtosecond time scale) from the ^{1}MLCT to the TiO_2 conduction band can occur.[41,79] For free $Ru^{II}(tpy)_2$, the ^{1}MLCT state reached after photoexcitation subsequently undergoes relaxation through intersystem crossing to a triplet excited state with a similar MO arrangement as the excited ^{1}MLCT state but with triplet character, i.e., a ^{3}MLCT state. For slow electron injection into TiO_2 (picosecond time scales) from thermally equilibrated triplet

Ru^{II}(tpy)$_2$ Dye-Sensitized TiO$_2$ Nanocrystals

J. Phys. Chem. B, Vol. 110, No. 41, 2006 **20517**

TABLE 1: Main Character of Highest Occupied and Lowest Unoccupied Molecular Orbitals of the Isolated Ru^{II}(tpy)$_2$ Derivatives[a]

molecular orbital	Ru^{II}(tpy)$_2$ [PF$_6^-$]$_2$	Ru^{II}(tpy)$_2$−COOH [PF$_6^-$]$_2$	Ru^{II}(tpy)$_2$−PO$_3$H$_2$ [PF$_6^-$]$_2$	Ru^{II}(tpy)$_2$−Ph−COOH [PF$_6^-$]$_2$	Ru^{II}(tpy)$_2$−Ph−PO$_3$H$_2$ [PF$_6^-$]$_2$	Ru^{II}(tpy)$_2$−Ph−COOH	Ru^{II}(tpy)$_2$−Ph−PO$_3$H$_2$
LUMO + 4	tpyI−π*	tpyI−π* + ca	tpyI−π* (pa)	tpyII−π*	tpyI−π* + Ph−π + pa		
LUMO + 3	tpyII−π*	tpyII−π*	tpyII−π*	Ph−π + ca (tpyI−π*)	tpyII−π*	tpyI−π* (tpyII−π* + Ru4d)	tpyI−π* (tpyII−π* + Ru4d)
LUMO + 2	tpy−π* (Ru4d)	tpyII−π* (Ru4d)	tpyII−π* (Ru4d)	tpyII−π* (Ru4d)	tpyII−π* (Ru4d)	tpyII−π* (tpyI−π*)	tpyII−π* (tpyI−π*)
LUMO + 1	tpyI−π*	tpyI−π*	tpyI−π*	tpyI−π*	tpyI−π*	tpyI−π* (Ph + ca + Ru4d)	tpyI−π* (Ph−π + Ru4d)
LUMO	tpyI−π* (Ru4d)	py2−π* + ca (Ru4d)	py2−π* (pa + Ru4d)	py2−π* + Ph−π + ca (Ru4d)	py2−π* + Ph−π (Ru4d)	tpyII−π* (Ru4d)	tpyII−π (Ru4d)*
HOMO	Ru4d	Ru4d	Ru4d	Ru4d	Ru4d	Ru4d + py2−π + Ph−π + ca	Ru4d + py2−π + Ph−π + pa
HOMO − 1	Ru4d	Ru4d (py5−π)	Ru4d (py5−π)	Ru4d (py5−π)	Ru4d (py5−π)	Ru4d (tpy−π)	Ru4d (tpy−π)
HOMO − 2	Ru4d (py2−π)	Ru4d (py2−π)	Ru4d (py2−π)	Ru4d (py2−π)	Ru4d (py2−π)	Ru4d (py5−π)	Ru4d (py5−π)
HOMO − 3	tpy−π	tpyII−π	tpyII−π	tpyII−π	tpyII−π	ca	pa + Ru4d
HOMO − 4	tpyI−π	tpyI−π	tpyI−π	tpyI−π	tpyI	Ph−π (Ru4d + ca)	pa (Ru4d)
HOMO − 5	tpyII−π			Ph−π (pa)	tpyII	Ph−π + Ru4d + ca (py2−π)	Ph−π (Ru4d)
HL gap[b,c]	3.21	2.83	3.03	2.98	3.04	3.33	3.32
d−d splitting[c]	5.59	5.58	5.60	5.59	5.59	5.45	5.46

[a] Minor contributions are included in parentheses. The labeling of the different parts of the dyes are: tpyI−tpy ligand with 4′-substituent; tpyII−tpy ligand with −H at the 4′-position; ca, carboxylate anchor; pa, phosphonate anchor; Ph, phenylene moiety; pyX−pyridyl with nitrogen number X according to Figure 1. [b] HOMO−LUMO gap. [c] In eV.

MLCT states,[41,79] the lifetime of the ^{3}MLCT state has to be sufficiently long-lived to initiate charge separation by ET from Ru^{II}(tpy)$_2$ to the TiO$_2$ acceptor before internal deactivation occurs.

One influence of the counterions on the MOs in the highest occupied and lowest unoccupied region for Ru^{II}(tpy)$_2$ is an energetic separation of MOs with orbital contribution localized on the two tpy ligands, tpyI and tpyII. Without counterions, orbital contributions are generally localized on both tpy ligands in a particular orbital. However, with inclusion of counterions, such orbitals are not found, and an orbital with contribution localized on tpyI becomes lower in energy than one with contribution on tpyII, which becomes higher in energy due to the proximity of the PF$_6^-$ ions.

Table 1 shows to what extent the anchor and spacer fragment MOs mix with the MO levels of the parent Ru^{II}(tpy)$_2$ complex. In the electronic structures, the carboxylic and phosphonic acid anchor fragments mix with the chromophore levels in the unoccupied orbitals in the LUMO and in LUMO + 3 or LUMO + 4 when two PF$_6^-$ are included. A significant anchor contribution is found in the LUMO level for Ru^{II}(tpy)$_2$−COOH, with a slight delocalization of the tpy−π* down to the anchor. This type of delocalization is also seen in LUMO + 4. The three top HOMOs of d-orbital type are largely unaffected by substitution at the 4′-position, both by anchor and spacer groups. The phenylene spacer orbitals mix with the Ru^{II}(tpy)$_2$ MO levels similarly to the anchor group orbitals, i.e., in LUMO and in LUMO + 3 or LUMO + 4. In the LUMO of Ru^{II}(tpy)$_2$−Ph−COOH and Ru^{II}(tpy)$_2$−Ph−PO$_3$H$_2$, there is a delocalization of the tpy−π* onto the phenylene spacer. Even though the phenyl plane is twisted out of the tpy plane, there is a partial delocalization over the two moieties. In Ru^{II}(tpy)$_2$−Ph−COOH, the LUMO is delocalized from the tpy over the Ph moiety and down to the anchor.

The character of the HOMO and LUMO of Ru^{II}(tpy)$_2$−Ph−COOH and Ru^{II}(tpy)$_2$−Ph−PO$_3$H$_2$ is found to be strongly affected by the inclusion or exclusion of counterions in the calculation. With counterions, the HOMO is foremost the d-orbital, and the LUMO consists of tpy−π*, Ph−π*, and anchor contributions (as mentioned above). However, without counterions, the orbitals of the phenylene unit mix into the HOMO, which contains a mixture of chromophore, spacer, and anchor contributions. The LUMO has instead only tpy−π* character on the remote tpy ligand (tpyII). The effect of counterions on HOMO and LUMO is seen in both the VD(T)Z and LANL2DZ electronic structures and is therefore unlikely to be a basis set effect. This variation in orbital delocalization found with and without counterions could result in different interpretations of the photoexcitation process (see further below).

When counterions are included in the calculations, all the energies of the MOs are upshifted; for instance, the HOMO for Ru^{II}(tpy)$_2$ is shifted from −11.2 to −6.4 eV when the counterions are included. The counterions balance the positive charges of the ruthenium ions, similarly to what is seen when including surroundings in the form of PCM solvent models.[80] For Ru^{II}(tpy)$_2$, the HOMO shifts from −11.2 to −6.2 eV in acetonitrile solvent calculated as a standard PCM single point calculation with VD(T)Z. The VD(T)Z-calculated HOMO− LUMO gap for Ru^{II}(tpy)$_2$ is 3.21 eV including PF$_6^-$, and 3.45 eV without. Hence, the HOMO−LUMO gap is decreased 0.2− 0.4 eV by inclusion of counterions (which is not seen using solvent model). Attachment of anchor and spacer groups results in a 0.1−0.4 eV decrease of the gap, where the largest decrease is seen for [Ru^{II}(tpy)$_2$−Ph−COOH][PF$_6^-$]$_2$.

Another interesting property of the electronic structure of Ru-polypyridyl coordination complexes such as Ru^{II}(tpy)$_2$ is the ligand field splitting, i.e., the splitting of the five degenerate Ru-4d orbitals in the free Ru atom into three occupied (t$_{2g}$) and
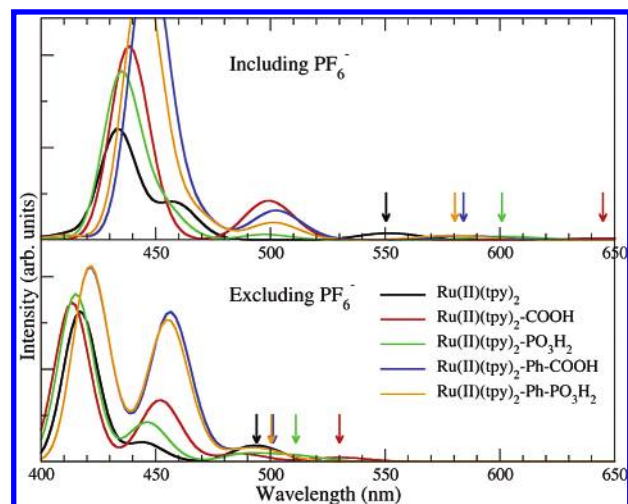
Figure 2. Simulated absorption spectra of the isolated $Ru^{II}(tpy)_2$ derivatives including two PF_6^- ions in the TD calculations (top) and excluding PF_6^- ions (bottom). The arrows indicate the lowest energy excitations.

two unoccupied (e_g) levels when interacting with the ligands. The size of this d–d splitting is believed to be related to the relative stability of the excited ^{3}MLCT state and a metal-centered triplet excited state, ^{3}MC, a state through which deactivation of the ^{3}MLCT state occurs.[78] Hence, the d–d splitting is believed to be important for the excited-state lifetime of Ru^{II}-$(tpy)_2$. In all systems, the lowest energy d–d splitting is 5.6 eV, which is the splitting between the d_{xy} and $d_{x^2-y^2}$ orbitals. The d–d splittings without counterions are slightly smaller. The results indicate that the anchor and spacer substitution will have very little effect on the excited-state lifetime through ^{3}MLCT → ^{3}MC deactivation.

3.1.3. Electronic Excitations and Absorption Spectra. The TD-B3LYP/VD(T)Z-simulated absorption spectra (400–650 nm) of the parent $Ru^{II}(tpy)_2$ and its four substituted derivatives are shown in Figure 2. In the top panel, the calculated spectra including explicit counterions are shown, while the lower panel shows the spectra excluding counterions. The calculated composition of the excitations responsible for key spectral features is listed in Table 2. The TD-B3LYP/VD(T)Z-calculated spectrum of $Ru^{II}(tpy)_2$ agrees well with the previously reported TD-B3LYP/LANL2DZ spectrum.[18] The simulated TD-B3LYP/VD(T)Z spectrum is shown in black in the lower graph of Figure 2. The shapes and features of the LANL2DZ and VD(T)Z spectra are highly similar, but the VD(T)Z excitations are slightly shifted (6–12 nm) to shorter wavelengths. Thus, the results indicate that TD-B3LYP/VD(T)Z performs as accurately as the commonly used TD-B3LYP/LANL2DZ. In fact, test calculations of the spectrum of $Ru^{II}(tpy)_2$ showed that the VD-(T)Z spectrum is highly similar (±3 nm) to that obtained with the large all-electron basis set 6-31+G(d,p), including both diffuse and polarization function, both calculations performed with LANL2DZ on Ru. The experimental MLCT absorption maximum at 470–475 nm[77,81,82] is not entirely reproduced for $Ru^{II}(tpy)_2$ by either TD-B3LYP/VD(T)Z or TD-B3LYP/LANL2DZ. The calculated VD(T)Z maximum at 418 nm is shifted ca. 50 nm to shorter wavelengths (corresponding to ca. 0.35 eV) relative to experiments. There are two less-intense peaks calculated at 445 and 494 nm that are closer to 470 nm that perhaps could be responsible for the experimental absorption maximum. However, in the comparison of spectra for the substituted complexes, where the relative shift between the complexes is of more importance, we expect significant cancel-

lation of the shift in absorption maximum between experiments and calculations. The inclusion of PF_6^- counterions in the calculations (top graph in Figure 2) shifts all spectral features in the 400–650 nm range toward longer wavelengths. The two $Ru^{II}(tpy)_2$ peaks at 418 and 445 nm are shifted to 434 and 459 nm, respectively. Moreover, the calculated absorption threshold, i.e., the lowest energy excitation, is shifted as much as 57 nm (corresponding to 0.26 eV). The corresponding shifts for the spectrum calculated with acetonitrile solvent included as a standard single point PCM calculation are 0–3 nm. Hence, it appears that the inclusion of surroundings in the calculations in the form of counterions give results in closer agreement with experiments. Effects of anchor and spacer group substitution on the spectra including explicit PF_6^- counterions will now be discussed (Figure 2, top).

The calculated absorption threshold, i.e., the lowest energy excitation, is of strong HOMO → LUMO character for all complexes. In $Ru^{II}(tpy)_2$, this is a d → tpy–π^* excitation. In the substituted complexes, this transition is also to anchor and spacer MO contributions. The transition has no calculated intensity and is therefore highlighted with colored arrows in the spectra in Figure 2. This lowest excitation is strongly shifted toward longer wavelengths in the substituted complexes compared to that of $Ru^{II}(tpy)_2$. For the phenylene-containing complexes, the shift is ca. 30 nm (0.12 eV). However, for the complexes with an anchor group directly attached to the tpy ligand, the shift is as large as 50 and 95 nm (0.19 and 0.33 eV) for $Ru^{II}(tpy)_2$–PO_3H_2 and $Ru^{II}(tpy)_2$–COOH, respectively. At first sight, the peak around 500 nm of the substituted complexes, containing a mixture of HOMO → LUMO + 1 (d → tpyI–π^*) and HOMO − 2 → LUMO (d → tpy–π^* + Ph + anchor), does not appear to have any match in the $Ru^{II}(tpy)_2$ spectrum. However, the calculated spectrum of $Ru^{II}(tpy)_2$ contains an excitation at 493 nm with the same character but with zero oscillator strength. In the 400–480 nm region, the simulated spectrum of $Ru^{II}(tpy)_2$ shows two peaks, at 434 and 459 nm, while the substituted complexes only have one peak. However, the peak of the substituted complexes contains two major excitations, one strong at 435–447 nm, and one less intense at 445–466 nm. The most intense excitation consists of a mixture of HOMO − 2 → LUMO, HOMO → LUMO + 1, and HOMO − 1 → LUMO + 2, and the less intense is mostly a HOMO − 2 → LUMO transition. For the phenylene-containing complexes, the 434 nm peak of $Ru^{II}(tpy)_2$ is shifted 10–13 nm toward longer wavelengths. The 459 nm excitation is shifted 5–14 nm to shorter wavelengths when the anchor group is directly attached to the tpy ligand, and shifted 7 nm to longer wavelengths when the complex contains a phenylene spacer.

Overall, the spectral features in the 400–650 nm range are mostly preserved upon substitution, merely slightly shifted toward longer wavelengths, and the relative intensity of different excitations are changed somewhat. Except for the lowest excited state, the spectral shifts caused by substitution are between −14 and +13 nm. The calculated results indicate that the experimental spectra would be very similar to the parent chromophore, hence an experimental spectral distinction would be difficult.

All calculated transitions in the 400–650 nm region are MLCT transitions, i.e., excitations from metal d-orbital to ligand tpy–π^* orbital. Moreover, in the substituted complexes, there is a significant portion of transitions from metal d-orbital to the LUMO in the lowest energy excitation and in the excitations around 498–503 nm and 435–447 nm. Because the ligand tpy–π^* orbital contributions in the LUMO of these complexes are partially conjugated with orbital contributions localized on the

TABLE 2: Selected Calculated Excitations Responsible for Key Spectral Features between 400 and 650 nm

	no.	wavelength (nm)	oscillator strength	main contributions
Ru^{II}(tpy)$_2$	1	493.5	0.0101	H − 0 → L + 0 (95%)
	2	493.5	0.0101	H − 0 → L + 1 (95%)
	5	444.6	0.0237	H − 0 → L + 2 (34%) H − 2 → L + 1 (30%) H − 1 → L + 0 (30%)
	7	417.6	0.1458	H − 0 → L + 2 (62%) H − 2 → L + 1 (14%) H − 1 → L + 0 (14%)
Ru^{II}(tpy)$_2$ [PF$_6^-$]$_2$	1	551.2	0.0083	H − 0 → L + 0 (94%)
	3	492.9	0.0000	H − 0 → L + 1 (77%) H − 2 → L + 0 (22%)
	5	459.1	0.0385	H − 2 → L + 1 (94%)
	7	433.5	0.1370	H − 2 → L + 0 (43%) H − 1 → L + 2 (31%) H − 0 → L + 1 (13%)
Ru^{II}(tpy)$_2$−COOH [PF$_6^-$]$_2$	1	645.5	0.0022	H − 0 → L + 0 (94%)
	3	499.2	0.0491	H − 0 → L + 1 (50%) H − 2 → L + 0 (44%)
	5	445.0	0.0292	H − 2 → L + 1 (93%)
	7	437.6	0.2160	H − 0 → L + 1 (42%) H − 2 → L + 0 (27%) H − 1 → L + 2 (16%)
Ru^{II}(tpy)$_2$−PO$_3$H$_2$ [PF$_6^-$]$_2$	1	600.9	0.0044	H − 0 → L + 0 (94%)
	3	497.9	0.0068	H − 0 → L + 1 (70%) H − 2 → L + 0 (28%)
	5	453.8	0.0349	H − 2 → L + 1 (93%)
	7	434.9	0.2046	H − 2 → L + 0 (40%) H − 0 → L + 1 (22%) H − 1 → L + 2 (20%)
Ru^{II}(tpy)$_2$−Ph−COOH [PF$_6^-$]$_2$	1	583.9	0.0051	H − 0 → L + 0 (91%)
	3	502.5	0.0367	H − 0 → L + 1 (62%) H − 2 → L + 0 (34%)
	5	466.1	0.0315	H − 2 → L + 1 (94%)
	7	446.9	0.3514	H − 2 → L + 0 (38%) H − 0 → L + 1 (31%) H − 1 → L + 2 (17%)
Ru^{II}(tpy)$_2$−Ph−PO$_3$H$_2$ [PF$_6^-$]$_2$	1	578.2	0.0056	H − 0 → L + 0 (93%)
	3	501.3	0.0216	H − 0 → L + 1 (67%) H − 2 → L + 0 (31%)
	5	466.4	0.0324	H − 2 → L + 1 (94%)
	7	444.1	0.3261	H − 2 → L + 0 (40%) H − 0 → L + 1 (26%) H − 1 → L + 2 (20%)

[a] For every transition, the principal one-electron transitions that contribute to the excitation and their relative contribution in percentage are given, where H = HOMO and L = LUMO.
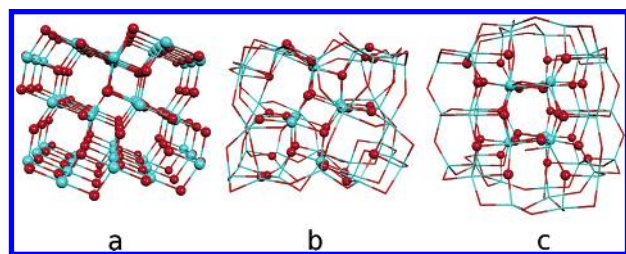

Figure 3. Geometry of the unrelaxed cluster (crystal structure coordinates) (a). Geometry of the optimized bare (TiO$_2$)$_{46}$ cluster, in side and top view, respectively (b and c). The total geometry in b and c is shown by a stick representation, and the fully coordinated Ti and O atoms are highlighted by a ball-and-stick representation.

Figure 4. Ti−O distance distribution of the optimized bare (TiO$_2$)$_{46}$ cluster.

spacer and anchor group moieties, the calculations indicate that anchor and spacer can mediate the electron transfer from metal to substrate.

The inclusion of explicit counterions in the calculations shifts all the spectral features of all the substituted complexes toward longer wavelengths (see Figure 2), as already mentioned above for the parent complex. In addition, for Ru^{II}(tpy)$_2$−Ph−COOH and Ru^{II}(tpy)$_2$−Ph−PO$_3$H$_2$, another significant difference is seen in the nature of the excitations when including or excluding counterions. With counterions, all excitations result in metal-to-ligand or metal-to-ligand−spacer−anchor excitations. Without counterions, the lowest energy excitation is dominated by metal−spacer−anchor-to-ligand transitions, thus indicating an excitation away from the substrate surface, which is clearly unwanted in terms of dye sensitization.

3.2. TiO$_2$ Nanocrystal. *3.2.1. Geometry.* Nanostructured TiO$_2$ is modeled by a (TiO$_2$)$_{46}$ cluster model, which is treated as a bare and charge neutral cluster. Central to our approach is a full geometry optimization of the TiO$_2$ nanoparticle model starting from a geometry constructed from crystal structure coordinates. The geometry of both the unrelaxed and the optimized (TiO$_2$)$_{46}$ models are displayed in Figure 3. In parts a and b of Figure 3, the typical anatase structural patterns and the sawtooth shape of the anatase (101) surface can be seen. In
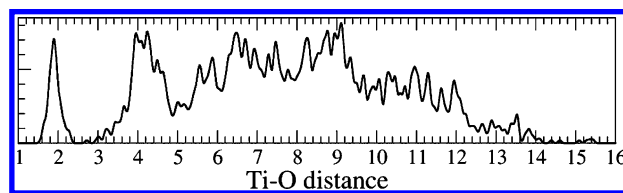
the anatase bulk structure, every Ti atom is coordinated by six O atoms, and every O atom by three Ti atoms. In the (TiO$_2$)$_{46}$ starting structure, already 60% of the atoms are undercoordinated, and therefore the geometry optimization causes considerable structural relaxation in the optimized structure. Although there is a high degree of structural reorganization, in which the connectivity is changed toward lower coordination, the anatase crystal form is largely preserved. A previous computational study of a wide range of bare TiO$_2$ clusters showed that the B3LYP/VDZ computational method tends to produce geometries with a high degree of surface reorganization and with lower total coordination than the crystal connectivity.[37] However, the study also showed that the potential energy surface for isomers with different bonding arrangements is relatively flat.

The (TiO$_2$)$_{46}$ cluster model has a quite spherical geometry (see Figure 3b and c), and therefore the cluster has a bulklike core, with six 6-fold-coordinated titanium atoms and a number of 3-fold-coordinated oxygens, which are highlighted in the figure.

Upon structural relaxation, the average Ti−O bond distance decreases from 1.95 to 1.91 Å. In Figure 4, the Ti−O distance distribution of the optimized (TiO$_2$)$_{46}$ cluster model is plotted. The plot reveals that the maximum Ti and O distance is 15.4 Å, which means that the cluster is nanosized. The maximum atom−atom distance is 16.5 Å. While the unrelaxed crystal bulk structure has two different bond lengths, the plot in Figure 4 reveals a Ti−O bond length spread of 1.5−2.3 Å for the optimized structure. The shortest Ti−O bonds result from the formation of Ti=O surface species during the optimization. Ti=
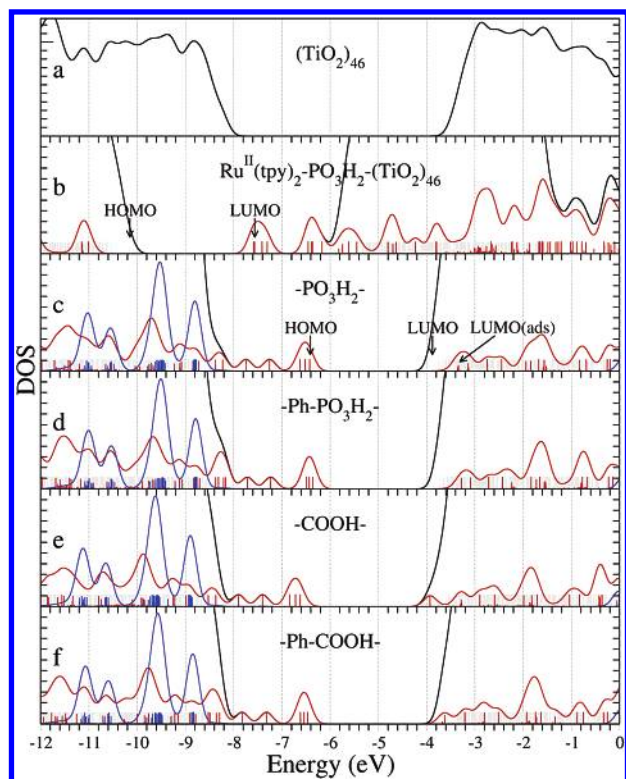
Figure 5. Total DOS (black curve and gray lines) and adsorbate (red) and PF_6^- (blue) projected DOS for (a) bare $(TiO_2)_{46}$, (b) $Ru^{II}(tpy)_2-PO_3H_2-(TiO_2)_{46}$ excluding counterions, (c) $Ru^{II}(tpy)_2-PO_3H_2-(TiO_2)_{46}$, (d) $Ru^{II}(tpy)_2-Ph-PO_3H_2-(TiO_2)_{46}$, (e) $Ru^{II}(tpy)_2-COOH-(TiO_2)_{46}$, and (f) $Ru^{II}(tpy)_2-Ph-COOH-(TiO_2)_{46}$, including counterions.

O sites are found not only at the surface edges but also in the center of the relatively stable (101) surface[83–85] with Ti=O bond lengths of 1.64 Å. Because approximately half of the atoms of the anatase (101) surface section in the $(TiO_2)_{46}$ cluster also are edge atoms, there is a lack of structural stabilization of the surface and a high degree of dangling bonds, which give rise to the Ti=O defect sites. Because of the Ti=O sites, there is an enhanced reactivity at the (101) surface.

Structural data that can be used to validate the quality of the calculated geometries, i.e., experimental Ti–O bond lengths, are not readily available. Instead, we have to rely on data of a single TiO_2 gas-phase molecule or of anatase bulk data. For a single TiO_2 gas-phase molecule, the B3LYP/VDZ geometry slightly underestimates the Ti–O distance, calculated to be 1.603 Å compared to the experimental 1.62 ± 0.08 Å.[86] The more accurate B3LYP/6-31G(d,p) predicts the Ti–O distance to be 1.630 Å. For anatase bulk, the two bulk Ti–O bond lengths are slightly overestimated by B3LYP/VDZ, 1.958 and 1.983 Å (VDZ)[25] compared to the crystal structure values 1.934 and 1.979 Å[61] or 1.937 and 1.965 Å.[87] The calculated VDZ bulk bond lengths are as good as those calculated with B3LYP and a modified 6-31G basis set by Beltran et al. (1.951 and 1.997 Å).[83]

3.2.2. Electronic Structure. The electronic structure for the fully optimized $(TiO_2)_{46}$ nanoparticle is described by B3LYP/VD(T)Z. Although $(TiO_2)_{46}$ is a finite cluster and not an infinite bulk crystal, i.e., the electronic structure consists of finite MO levels and not continuous bands, we adopt the language of solids. The spacing of the MO levels in the lower unoccupied region (which is relevant for the discussion in Section 3.3) is on average of the order of 20 meV, including all unoccupied levels up to −3.0 eV. However, in the very lowest levels, the spacing is sparse (up to maximum 70 meV). Figure 5a shows the

constructed efficient density of states (DOS) obtained by a 0.3 eV artificial Gaussian broadening of the individual MO levels. The nanoparticle exhibits a broad, filled valence band (VB) and a broad, empty conduction band (CB), which are separated by a defect-free band gap. The top of the VB essentially consists of oxygen 2p orbital character, whereas the CB is mainly of titanium 3d orbital character. The DOS plot in Figure 5a shows that there are no states in the band gap region. The calculated HOMO−LUMO (electronic) band gap is 4.7 eV, while the calculated optical band gap, i.e., the lowest TD-DFT excitation, is 4.0 eV. The electronic and optical VD(T)Z gaps are highly similar to those calculated with the VDZ basis set. The B3LYP/VDZ calculated electronic bulk band gap is 3.4 eV,[25] which is a slight overestimation of the experimental band gap of 3.2 eV[84,88] for anatase bulk. Moreover, the band gap of a 2.4 nm TiO_2 nanoparticle has a 0.2 eV larger band gap than the bulk.[89] In addition, a previous study showed that a highly reorganized cluster model has a larger band gap than that of a less reorganized one. In that study, 0.6 eV (HOMO−LUMO) and 0.4 eV (TD) larger gaps were calculated for the $(TiO_2)_{46}$ model used in this study than that for a model more similar to the original cluster with bulk bond lengths. Therefore, we expect the HOMO−LUMO gap calculated here to be slightly overestimated.

Although the electronic and optical gaps are relatively insensitive to basis set choice, the positions of the VB and CB edges, i.e., the HOMO and LUMO levels, are more basis set sensitive.[37] The calculated HOMO level is −7.5 and −8.2 eV with the VDZ and VD(T)Z basis sets, respectively. The calculated LUMO level is −2.8 and −3.5 eV for the VD(T)Z and VD(T)Z basis set, respectively, which can be compared to the measured CB edge of TiO_2 of −4.4 eV.[4] Because the VD-(T)Z basis sets appears to give a LUMO level closer to experiments than VDZ, we use VD(T)Z to describe the dye-sensitized systems in Section 3.3.

3.3. Dye-Sensitized Nanocrystal. *3.3.1. Adsorption.* The adsorption of the substituted $Ru^{II}(tpy)_2$ dyes onto TiO_2 anatase nanoparticles was studied by first adsorbing the anchor groups. The B3LYP/VDZ-optimized geometry of phosphonic and carboxylic acids adsorbed in a monodentate mode on the $(TiO_2)_{46}$ cluster, $HPO_3H_2-(TiO_2)_{46}$ and $HCOOH-(TiO_2)_{46}$, has previously been described in detail.[37] The separately optimized $Ru^{II}(tpy)_2$ dyes, including two PF_6^- counterions, were mounted on the anchor acid−$(TiO_2)_{46}$ structures as described in Section 2 (Methods), and the resulting structures, $Ru^{II}(tpy)_2-PO_3H_2-(TiO_2)_{46}$, $Ru^{II}(tpy)_2-COOH-(TiO_2)_{46}$, $Ru^{II}(tpy)_2-Ph-PO_3H_2-(TiO_2)_{46}$, and $Ru^{II}(tpy)_2-Ph-COOH-(TiO_2)_{46}$, are shown in Figure 6. The monodentate adsorption via the phosphonic acid consists of three adsorbate−substrate bonds, a long $Ti-O_{ads}$ of 2.00 Å, and two shorter $O_{sub}-HO_{ads}$ of 1.51 and 1.58 Å. The monodentate adsorption via the carboxylic acid consists of two adsorbate−substrate bonds, a long $Ti-O_{ads}$ of 2.07 Å and a short $O_{sub}-HO_{ads}$ of 1.35 Å. Because VDZ predicts even longer Ru−N bonds than LANL2DZ (0.02 Å), the latter is used for the description of the geometry of $Ru^{II}(tpy)_2$ and spacer moieties. The very small overall geometric changes found when connecting the chromophore−spacer−anchor parts (discussed in Section 3.1.1) is reassuring with respect to the composite optimization scheme employed.

The adsorption energies are calculated to be 81 and 82 kcal/mol for $Ru^{II}(tpy)_2-PO_3H_2-(TiO_2)_{46}$ and $Ru^{II}(tpy)_2-Ph-COOH-(TiO_2)_{46}$, respectively, and 38 and 39 kcal/mol for $Ru^{II}(tpy)_2-COOH-(TiO_2)_{46}$ and $Ru^{II}(tpy)_2-Ph-COOH-(TiO_2)_{46}$, respectively. The calculated adsorption energies of the

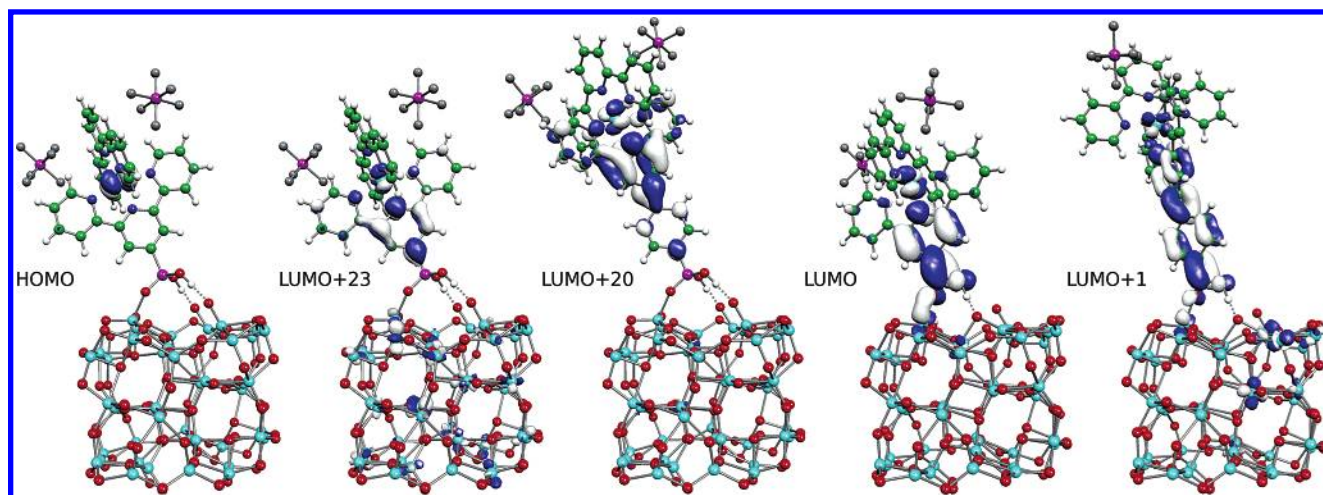**Figure 6.** Highest occupied (HOMO) of Ru^{II}(tpy)$_2$−PO$_3$H$_2$−(TiO$_2$)$_{46}$ and selected lowest unoccupied (LUMO) molecular orbital for Ru^{II}(tpy)$_2$−PO$_3$H$_2$−(TiO$_2$)$_{46}$, Ru^{II}(tpy)$_2$−COOH−(TiO$_2$)$_{46}$, Ru^{II}(tpy)$_2$−Ph−PO$_3$H$_2$−(TiO$_2$)$_{46}$, and Ru^{II}(tpy)$_2$−Ph−COOH−(TiO$_2$)$_{46}$, including counterions.

TABLE 3: Calculated HOMO and LUMO Energies, and HOMO−LUMO (HL) and Optical (TD) Band Gaps in eV

	E_{HOMO} (free)	E_{HOMO}	E_{CB} (E_{LUMO})	HL gap	TD gap
(TiO$_2$)$_{46}$		−8.18	−3.47	4.71	3.97
HPO$_3$H$_2$−(TiO$_2$)$_{46}$		−8.24	−3.60	4.64	
HCOOH−(TiO$_2$)$_{46}$		−8.13	−3.51	4.62	
Ru^{II}(tpy)$_2$−PO$_3$H$_2$−(TiO$_2$)$_{46}$ excl. PF$_6^-$	−11.23	−10.17	−5.82 (−7.59)	2.58	
Ru^{II}(tpy)$_2$−PO$_3$H$_2$−(TiO$_2$)$_{46}$	−6.52	−6.42	−3.34	2.55	2.11
Ru^{II}(tpy)$_2$−Ph−PO$_3$H$_2$−(TiO$_2$)$_{46}$	−6.42	−6.36	−3.28	2.59	2.17
Ru^{II}(tpy)$_2$−COOH−(TiO$_2$)$_{46}$	−6.57	−6.62	−3.89	2.69	1.84
Ru^{II}(tpy)$_2$−Ph−COOH−(TiO$_2$)$_{46}$	−6.42	−6.47	−3.62	2.79	2.07

dyes adsorbed on the TiO$_2$ nanoparticle are highly similar to those when only the anchor groups are adsorbed, with a stronger binding for the phosphonic anchoring. This result is in agreement with previous studies, experimental and computational, which indicates that an adsorbate binds stronger via phosphonic acid than via carboxylic acid.[25,37,90−94]

3.3.2. Interfacial Electronic Structure. In the electronic structure of HPO$_3$H$_2$−(TiO$_2$)$_{46}$ and HCOOH−(TiO$_2$)$_{46}$, all the anchor group MO levels are well merged into the substrate VB and CB, indicating strong electronic coupling to the surface. As shown in Table 3, the adsorption of the anchor groups does not shift or change the size of the band gap compared to the bare TiO$_2$ cluster.

The DOS for the bare and dye-sensitized (TiO$_2$)$_{46}$ clusters are presented in Figure 5 along with the adsorbate-projected DOS (PDOS) shown in red. When adsorbing the doubly charged Ru^{II}(tpy)$_2$ dyes on (TiO$_2$)$_{46}$ without inclusion of counterions, all the substrate levels shift compared to the bare cluster. In Figure 5b, the calculated DOS for Ru^{II}(tpy)$_2$−PO$_3$H$_2$−(TiO$_2$)$_{46}$ excluding counterions show how all the TiO$_2$ MO levels are downshifted ca. 2 eV compared to the bare cluster in Figure 5a. However, the band gap is intact, as seen in Table 3. The energy of the adsorbate levels are maintained upon adsorption (shift < 0.3 eV), which results in no occupied adsorbate MO in the band gap, but several unoccupied adsorbate MOs below the CB edge. The position of the adsorbate HOMO and LUMO levels are indicated in Figure 5b. Clearly, there is no coupling between the unoccupied LUMO and the substrate CB contrary to what is expected. As seen in Section 3.1.2, the inclusion of explicit counterions raises the MO energy of the free dyes about 4−5 eV. When adsorbing the Ru^{II}(tpy)$_2$ dyes on TiO$_2$ with inclusion of counterions, the adsorbate levels are energetically maintained and, moreover, are also all the TiO$_2$ levels qualitatively preserved as for the bare cluster, see Figure 5. A comparison of the results for Ru^{II}(tpy)$_2$−PO$_3$H$_2$−

(TiO$_2$)$_{46}$ with and without inclusion of counterions shows that the size of the band gap is intact but there is a difference in the CB edge energy of ca. 2 eV, as seen in Table 3. The counterion PDOS is shown in blue in Figure 5. The counterions introduce occupied levels in the substrate VB slightly below the VB edge and unoccupied levels well above the CB edge. Hence, the photoexcitation and the electron-injection processes do not appear to be affected by inclusion of counterions. The problem of level alignment for charged dyes interacting with a neutral substrate could also possibly be remedied by inclusion of a solvent.[80] In all of our calculations, we have used two PF$_6^-$ counterions. Further discussions are based on results including counterions unless otherwise indicated.

The reported DOS and PDOS for Ru^{II}(tpy)$_2$−PO$_3$H$_2$−(TiO$_2$)$_{46}$, Ru^{II}(tpy)$_2$−COOH−(TiO$_2$)$_{46}$, Ru^{II}(tpy)$_2$−Ph−PO$_3$H$_2$−(TiO$_2$)$_{46}$, and Ru^{II}(tpy)$_2$−Ph−COOH−(TiO$_2$)$_{46}$ are shown in Figure 5c−f. All four adsorbates introduce occupied levels in the lower region of the substrate band gap, which become the highest occupied levels in their respective systems. The five highest occupied levels correspond to the five highest occupied levels of the free adsorbates and are entirely localized on the adsorbates, as exemplified by the HOMO of Ru^{II}(tpy)$_2$−PO$_3$H$_2$−(TiO$_2$)$_{46}$ shown on the left in Figure 6. The three highest occupied are the Ru 4d orbitals: d$_{xy}$ (HOMO), d$_{xz}$ (HOMO − 1), and d$_{yz}$ (HOMO − 2). The two following levels, HOMO − 3 and HOMO − 4, are tpy−π orbitals.

The LUMO of Ru^{II}(tpy)$_2$−PO$_3$H$_2$−(TiO$_2$)$_{46}$ and Ru^{II}(tpy)$_2$−Ph−PO$_3$H$_2$−(TiO$_2$)$_{46}$ are totally localized on the metal oxide, see Figure 5c,d. In Ru^{II}(tpy)$_2$−COOH−(TiO$_2$)$_{46}$ and Ru^{II}(tpy)$_2$−Ph−COOH−(TiO$_2$)$_{46}$, on the other hand, the energies of the LUMO from the isolated adsorbate and the edge of the TiO$_2$ CB coincides, and therefore the LUMO of the adsorbate−substrate system contain contributions from both adsorbate and substrate.

TABLE 4: Five Lowest Energy Excitations Calculated for the Four Ru^{II}(tpy)$_2$-sensitized (TiO$_2$)$_{46}$ Systems Including Counterions

	no.	wavelength (nm)	oscillator strength	main contributions	$p_i{}^a$/level^b
Ru^{II}(tpy)$_2$−PO$_3$H$_2$−(TiO$_2$)$_{46}$	1	587.9	0.0043	H − 0 → L + 23 (39%) H − 0 → L + 21 (30%) H − 0 → L + 20 (7%)	0.48/1 0.37/1 0.10/1
	2	571.6	0.0000	H − 1 → L + 23 (40%) H − 1 → L + 21 (31%) H − 1 → L + 20 (8%)	0.48/1 0.37/1 0.10/1
	3	531.8	0.0000	H − 0 → L + 0 (96%)	0.00/-
	4	518.4	0.0000	H − 0 → L + 1 (98%)	0.00/-
	5	510.5	0.0000	H − 1 → L + 0 (96%)	0.00/-
Ru^{II}(tpy)$_2$−Ph−PO$_3$H$_2$−(TiO$_2$)$_{46}$	1	570.3	0.0058	H − 0 → L + 20 (84%)	0.92/1
	2	559.6	0.0000	H − 1 → L + 20 (85%)	0.92/1
	3	511.1	0.0000	H − 0 → L + 0 (99%)	0.00/-
	4	500.0	0.0000	H − 0 → L + 1 (100%)	0.00/-
	5	495.8	0.0000	H − 1 → L + 0 (99%)	0.00/-
Ru^{II}(tpy)$_2$−COOH−(TiO$_2$)$_{46}$	1	675.4	0.0014	H − 0 → L + 0 (88%)	0.90/1
	2	649.8	0.0000	H − 1 → L + 0 (89%)	0.90/1
	3	511.4	0.1662	H − 2 → L + 0 (52%) H − 0 → L + 20 (21%) H − 0 → L + 21 (11%) H − 0 → L + 18 (5%)	0.90/1 0.58/2 0.34/2 0.17/2
	4	472.1	0.0002	H − 0 → L + 1 (96%)	0.03/-
	5	463.0	0.0000	H − 0 → L + 2 (97%)	0.01/-
Ru^{II}(tpy)$_2$−Ph−COOH−(TiO$_2$)$_{46}$	1	599.0	0.0038	H − 0 → L + 1 (63%) H − 0 → L + 0 (15%)	0.74/1 0.18/1
	2	585.4	0.0000	H − 1 → L + 1 (62%) H − 1 → L + 0 (14%)	0.74/1 0.18/1
	3	508.6	0.1057	H − 0 → L + 19 (52%) H − 2 → L + 1 (30%) H − 2 → L + 0 (8%)	0.99/2 0.74/1 0.18/1
	4	484.9	0.0002	H − 1 → L + 19 (96%)	0.99/2
	5	471.2	0.0001	H − 0 → L + 0 (83%) H − 0 → L + 1 (15%)	0.18/1 0.74/1

^{a} p_i is the portion of adsorbate centered MO contributions. ^{b} Level denotes the first or second LUMO (ads) levels (LUMO (ads) and LUMO + 1 (ads), respectively).

The efficiency of excited-state ET into the TiO$_2$ CB depends on the spatial and energetic overlap of the lowest unoccupied adsorbate MOs with the CB. The calculated MO levels of the sensitized TiO$_2$ that have nonnegligible contributions from the free adsorbate LUMO are collectively referred to as LUMO (ads). For all systems, the LUMO (ads) levels have orbital contributions on Ru, the binding tpyI ligand, and the anchor group, as well as contributions on TiO$_2$ (see selected LUMO (ads) in Figure 6). The LUMO (ads) levels for Ru^{II}(tpy)$_2$−PO$_3$H$_2$ are situated higher up in the CB, which can be seen in the PDOS plot in Figure 5c. Moreover, the levels are spread over a significant portion of the substrate band, with a significant coupling to the TiO$_2$. The lowest LUMO (ads) levels for Ru^{II}-(tpy)$_2$−COOH are located at the edge of the CB in a region with large substrate level spacing. This means that there are no lower and few higher unoccupied TiO$_2$ levels to couple to, which leads to the lowest LUMO (ads) levels being spread out on a large region of few but widely separated levels instead of being spread out on a large region of several narrowly spaced levels. In this situation, the LUMO (ads) does not properly fulfill the criteria of being in the wide band limit, which probably makes the calculated interfacial electronic coupling more sensitive to the local geometry at the interface.

The calculated five lowest excitations for the dye-sensitized (TiO$_2$)$_{46}$ systems (including counterions) are listed in Table 4. The lowest energy excitation for all systems is of adsorbate-to-adsorbate character. For Ru^{II}(tpy)$_2$−PO$_3$H$_2$, the two lowest excitations are Ru 4d-orbital to LUMO + 20, LUMO + 21, and LUMO + 23 transitions. These three orbitals belong to the lowest LUMO (ads), and LUMO + 23 is shown in Figure 6. None of the five lowest excitations for Ru^{II}(tpy)$_2$−PO$_3$H$_2$ have significant oscillator strength. For Ru^{II}(tpy)$_2$−COOH, the two lowest excitations are of pure one-electron transitions from an adsorbate d-orbital to the LUMO. The third lowest excitation, at 511 nm, has significant intensity and consists of ca. 50% d-orbital to LUMO transition, but also of ca. 40% d-orbital to LUMO + 18, LUMO + 20, and LUMO + 21 type. The latter

corresponds to the second LUMO (ads), i.e., levels with significant contribution from the free adsorbate LUMO + 1, referred to as LUMO + 1 (ads) and found in the PDOS around −3.3 eV in Figure 5e.

For Ru^{II}(tpy)$_2$−Ph−PO$_3$H$_2$ and Ru^{II}(tpy)$_2$−Ph−COOH, the relative location of the LUMO (ads) levels is highly similar to the situation when the anchor is directly connected to the tpy ligand, as seen in Figure 5. The LUMO (ads) levels for Ru^{II}-(tpy)$_2$−Ph−PO$_3$H$_2$ are situated higher up in the CB, while the levels for Ru^{II}(tpy)$_2$−Ph−COOH are located at the edge of the CB where there are few and widely spaced levels, which again makes the calculation of electronic coupling more sensitive to, e.g., local structure. The introduction of a phenylene spacer weakens the interaction between the chromophore and the TiO$_2$ substrate, which can be seen as only a few narrow LUMO (ads) levels in the PDOS in Figure 5d,f. The two lowest calculated excitations for Ru^{II}(tpy)$_2$−Ph−PO$_3$H$_2$ are mainly from Ru 4d to LUMO + 20 (shown in Figure 6), which is the LUMO (ads) level with distinctly large adsorbate character. This is similar to the lowest excitations of Ru^{II}(tpy)$_2$−PO$_3$H$_2$, but with more single configuration character due to the weaker coupling of LUMO (ads) to the substrate. The calculated excitations for Ru^{II}-(tpy)$_2$−Ph−COOH are highly similar to those of Ru^{II}(tpy)$_2$−COOH. The two lowest excitations are to LUMO and LUMO + 1 (shown in Figure 6), i.e., the LUMO (ads) levels. The third excitation, which has significant oscillator strength, is 52% to LUMO + 19, which corresponds to LUMO + 1 (ads).

Additional information of the electronic coupling has also been extracted from constructed Lorentzian distributions of the LUMO (ads) levels. The resulting distributions are shown in Figure 7, together with the LUMO (ads) levels used in the construction. Note that, in the graphs for Ru^{II}(tpy)$_2$−PO$_3$H$_2$ and Ru^{II}(tpy)$_2$−Ph−PO$_3$H$_2$, the LUMO + 1 (ads) levels are present at ∼0.2 eV above the LUMO (ads) levels. In Table 5, the reported adsorbate-induced energy shift, ΔE, is +0.14 eV for Ru^{II}(tpy)$_2$−PO$_3$H$_2$ and −0.15 eV for Ru^{II}(tpy)$_2$−COOH, which possibly indicates a stronger electronic coupling of the LUMO

Ru^{II}(tpy)$_2$ Dye-Sensitized TiO$_2$ Nanocrystals

J. Phys. Chem. B, Vol. 110, No. 41, 2006 **20523**

TABLE 5: Calculated Adsorbate LUMO Energies, the Shift (ΔE), and Broadening (ℏΓ) of the Adsorbate LUMO and Estimated Injection Times

	E_{LUMO} (free ads)^a	E_{LUMO} (ads)^a	Δ$E^{a,b}$	ℏΓ (fwhm)^c	τ (fs)
Ru^{II}(tpy)$_2$−PO$_3$H$_2$−(TiO$_2$)$_{46}$	−3.48	−3.34	0.14	10.5	62 (152)^d
Ru^{II}(tpy)$_2$−Ph−PO$_3$H$_2$−(TiO$_2$)$_{46}$	−3.38	−3.28	0.10	4.2	158 (>1 ps)^d
Ru^{II}(tpy)$_2$−COOH−(TiO$_2$)$_{46}$	−3.74	−3.89	−0.15	69	9.5 (98)^d
Ru^{II}(tpy)$_2$−Ph−COOH−(TiO$_2$)$_{46}$	−3.44	−3.62	−0.18	26	25 (>1 ps)^d

^{a} Energy in eV. ^{b} Δ$E = E_{LUMO}$ (ads) − E_{LUMO} (free ads). ^{c} Energy in meV. ^{d} Injection time of adsorbate LUMO + 1.
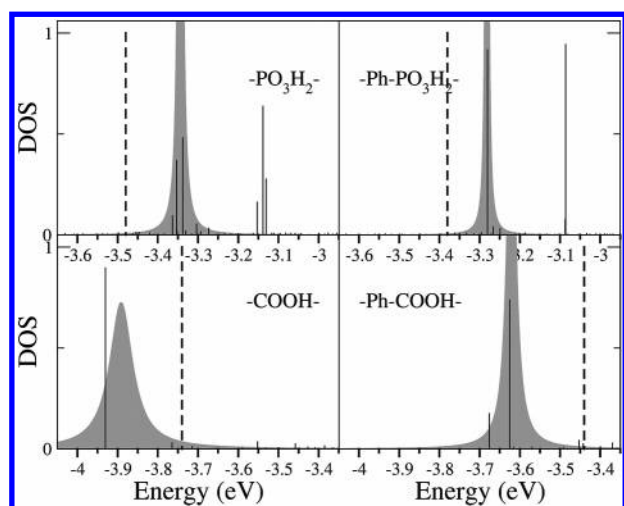

Figure 7. Plots of the Lorentzian distribution (curve) of the LUMO (ads) levels (lines) resulting from the splitting of the adsorbate LUMO in Ru^{II}(tpy)$_2$−PO$_3$H$_2$−(TiO$_2$)$_{46}$ (top left), Ru^{II}(tpy)$_2$−Ph−PO$_3$H$_2$−(TiO$_2$)$_{46}$ (top right), Ru^{II}(tpy)$_2$−COOH−(TiO$_2$)$_{46}$ (bottom left), and Ru^{II}-(tpy)$_2$−Ph−COOH−(TiO$_2$)$_{46}$ (bottom right). The dashed lines indicate the position of the LUMO(free) levels.

(ads) for Ru^{II}(tpy)$_2$−COOH. This mutual raising and lowering of the LUMO (ads) is maintained when connecting the phenylene spacers and are +0.10 and −0.18 eV for Ru^{II}(tpy)$_2$−Ph−PO$_3$H$_2$ and Ru^{II}(tpy)$_2$−Ph−COOH, respectively.

The electron injection times estimated from the Lorentzian lifetime broadening are reported in Table 5. The calculated injection times of LUMO (ads) are all in the sub-200 fs regime. There is a clear distinction between the two anchor groups, and the injection for the systems with carboxylic acid are much faster than those with the phosphonic acid. The calculations indicate that the introduction of the phenylene spacer group more than doubles the injection time.

Because the calculated excitations showed that also excitations to higher LUMO (ads) levels can be involved for Ru^{II}(tpy)$_2$−COOH and Ru^{II}(tpy)$_2$−Ph−COOH, the injection times of the second LUMO (ads) are also included in the table within parentheses. The calculated injection time of LUMO + 1 (ads) for Ru^{II}(tpy)$_2$−COOH−(TiO$_2$)$_{46}$ is again shorter than that for Ru^{II}(tpy)$_2$−PO$_3$H$_2$, and they are both much longer than those calculated for LUMO (ads). The significantly weaker electronic coupling of LUMO + 1 (ads) to the surface can be explained by the character of the free adsorbate LUMO + 1, which, contrary to LUMO, has no mixing of the tpy−π orbital and the anchor group. The introduction of a spacer group between the tpy ligand and the anchor group further increases the distance between the tpy ligand and the TiO$_2$ and therefore severely reduces the possibility of a tpy−π orbital delocalized on the surface. The electronic coupling of the LUMO + 1 (ads) in Ru^{II}(tpy)$_2$−Ph−COOH−(TiO$_2$)$_{46}$ and Ru^{II}(tpy)$_2$−Ph−PO$_3$H$_2$−(TiO$_2$)$_{46}$ are also much weaker than that for LUMO (ads), with calculated injection times exceeding 1 ps.

4. Conclusions

Electronic properties of dye-sensitized TiO$_2$ nanocrystals composed of a (TiO$_2$)$_{46}$ model nanocrystal and a set of Ru^{II}-(tpy)$_2$ dyes have been investigated using DFT and TD-DFT calculations.

The calculated electronic properties of both the isolated model TiO$_2$ nanocrystal and the isolated ruthenium dyes are found to be in reasonable agreement with published experimental information on the respective systems. The calculations of the combined system, however, show that it is important to include environmental effects, such as charge stabilization by, e.g., counterions, to realistically model the positions of the energy levels of the adsorbate relative to band edges of the fundamental band gap of the substrate. This effect is found to be much more important for the ruthenium dyes carrying a nominal net charge, compared to charge neutral adsorbates such as either organic chromophores or the formally neutral ruthenium dye N3 previously studied using a similar computational approach.[40] TD-DFT calculations of the isolated dye molecules showed an interesting reversal of the excitation direction when comparing systems including and excluding explicit counterions.

Comparing calculated interfacial electronic couplings for two different anchor groups as well as the effect of inserting a phenylene spacer group between the Ru^{II}(tpy)$_2$ chromophore and the anchor group, there is clear evidence that the interfacial coupling strength is significantly affected by the presence of both anchor and spacer groups. The calculations predict that the phosphonic acid anchor group decreases the interfacial electronic coupling by approximately a factor of 6.4, whereas the insertion of a phenylene group in each case decreases the coupling by a factor close to 2.6. Comparing the strongest coupling case with a carboxylic acid anchor and no spacer group to the weakest coupling case with the phosphonic acid anchor and the phenylene spacer, it appears tentatively as if the combined effects of the anchor and spacer groups on the electronic coupling are multiplicative, in the sense that, overall, the electronic coupling decreases by a factor of 16.6, which is virtually identical to the value close to 16.6 obtained by multiplying the individual factors of 2.6 and 6.4 together. The strong electronic coupling results in estimated electron injection times that are very fast. The injection times using the carboxylic acid as an anchor group are calculated to be twice as fast as those for the phosphonic anchor group. However, it appears to be a near band edge case for the carboxylic acid, where the lowest excited states (or more precisely LUMO (ads)) are situated very close or even somewhat below the CB edge. In such a case, the mechanism of the electron injection process may differ from the electron injection from the excited dye into a region of the CB, where the DOS is described by a continuum of levels instead of discrete levels. In this near-band edge region, other effects such as vibrational effects, Franck−Condon factors, and reorganization energies may influence the charge injection dynamics to a higher extent. Hence, the choice of the anchor group may not only have influence on the rate but also on the

mechanisms of the electron injection. In this paper, however, the emphasis is on the electronic coupling and other effects are not considered.

Explicit calculations of the lowest few excited states of the dye-sensitized systems were performed using TD-DFT calculations. In several cases, the lowest excited states were dominated by adsorbate−adsorbate transitions, although the overall lowest unoccupied orbitals for the dyes containing a phosphonic group are located in the substrate band. This indicates that biphasic injection kinetics could be expected in which excited states above the conduction band edge would inject electrons on an ultrafast time scale controlled by the interfacial coupling, while there could be a slower component from the red end of the absorption or from dye molecules that have time to undergo internal vibrational relaxation to the lowest excited singlet state on a time scale faster than the electron injection.

Because of the proximity in energy of the lowest excited states of the chromophores relative to the conduction band edge, this is in reality likely to be very sensitive also to other factors such as the size of the nanocrystals or the presence of a solvent. Further work to bring the quantum chemical calculations even closer to working experimental conditions in photoelectrochemical systems will therefore be important.

Supporting Information Available: Cartesian coordinates of geometry optimized free $Ru^{II}(tpy)_2$ dyes with explicit counterions and tables with geometry details (bond lengths and angles) of these geometries. Electronic structure details, including MO composition and selected excitations, of the free dyes calculated excluding counterions. This material is available free of charge via the Internet at http://pubs.acs.org.

References and Notes

(1) Kavarnos, G. J. *Fundamentals of Photoinduced Electron Transfer*; VCH Publishers: New York, 1993.

(2) Miller, R. J. D.; McLendon, G. L.; Nozik, A. J.; Schmickler, W.; Willig, F. *Surface Electron-Transfer Processes*; VCH Publishers: New York, 1995.

(3) Schnadt, J.; Bruhwiler, P. A.; Patthey, L.; O'Shea, J. N.; Södergren, S.; Odelius, M.; Ahuja, R.; Karis, O.; Bassler, M.; Persson, P.; Siegbahn, H.; Lunell, S.; Mårtensson, N. *Nature* **2002**, *418*, 620−623.

(4) Hagfeldt, A.; Grätzel, M. *Chem. Rev.* **1995**, *95*, 49−68.

(5) Alstrum-Acevedo, J. H.; Brennaman, M. K.; Meyer, T. J. *Inorg. Chem.* **2005**, *44*, 6802−6827.

(6) Brown, G. E., Jr.; Henrich, V. E.; Casey, W. H.; Clark, D. L.; Eggleston, C.; Telmy, A.; Goodman, D. W.; Grätzel, M.; Maciel, G.; McCarthy, M. I.; Nealson, K. H.; Sverjensky, D. A.; Toney, M. F.; Zachara, J. M. *Chem. Rev.* **1999**, *99*, 77−174.

(7) Grosshenny, V.; Harriman, A.; Ziessel, R. *Angew. Chem., Int. Ed. Engl.* **1995**, *34*, 1100−1102.

(8) Juris, A.; Balzani, V.; Barigelletti, F.; Campagna, S.; Belser, P.; von Zelevsky, A. *Coord. Chem. Rev.* **1988**, *84*, 85−277.

(9) Bonhote, P.; Moser, J.-E.; Humphry-Baker, R.; Vlachopoulos, N.; Zakeeruddin, S. M.; Walder, L.; Grätzel, M. *J. Am. Chem. Soc.* **1999**, *121*, 1324−2336.

(10) Ershov, A. Y.; Shashko, A. D.; Sizova, O. V.; Ivanova, N. V.; Burov, S. V.; Kuteikina-Teplyakova, A. V. *Russ. J. Gen. Chem.* **2003**, *73*, 135−140.

(11) Fantacci, S.; De Angelis, F.; Selloni, A. *J. Am. Chem. Soc.* **2003**, *125*, 4381−4387.

(12) Eskelinen, E.; Haukka, M.; Kinnunen, T. J. J.; Pakkanen, T. A. *J. Electroanal. Chem.* **2003**, *556*, 103−108.

(13) Singh, A.; Chandra, M.; Sahay, A. N.; Pandey, D. S.; Pandey, K. K.; Mobin, S. M.; Puerta, M. C.; Valerga, P. *J. Organomet. Chem.* **2004**, *689*, 1821−1834.

(14) Pourtois, G.; Beljonne, D.; Moucheron, C.; Schumm, S.; Kirsch-De Mesmaeker, A.; Lazzaroni, R.; Bredas, J. L. *J. Am. Chem. Soc.* **2004**, *126*, 683−692.

(15) Aiga, F.; Tada, T. *Sol. Energy Mater. Sol. Cells* **2005**, *85*, 437−446.

(16) Xie, Z. Z.; Fang, W. H. *J. Mol. Struct. (THEOCHEM)* **2005**, *717*, 179−187.

(17) Gorelsky, S. I.; Lever, A. B. P. *J. Organomet. Chem.* **2001**, *635*, 187−196.

(18) Zhou, X.; Ren, A. M.; Feng, J. K. *J. Organomet. Chem.* **2005**, *690*, 338−347.

(19) Amini, A.; Harriman, A.; Mayeux, A. *Phys. Chem. Chem. Phys.* **2004**, *6*, 1157−1164.

(20) Ciofini, I.; Laine, P. P.; Bedioui, F.; Adamo, C. *J. Am. Chem. Soc.* **2004**, *126*, 10763−10777.

(21) Charlot, M. F.; Pellegrin, Y.; Quaranta, A.; Leibl, W.; Aukauloo, A. *Chem.−Eur. J.* **2006**, *12*, 796−812.

(22) Nazeeruddin, M. K.; De Angelis, F.; Fantacci, S.; Selloni, A.; Viscardi, G.; Liska, P.; Ito, S.; Takeru, B.; Grätzel, M. G. *J. Am. Chem. Soc.* **2005**, *127*, 16835−16847.

(23) Villegas, J. M.; Stoyanov, S. R.; Huang, W.; Lockyear, L. L.; Reibenspies, J. H.; Rillema, D. P. *Inorg. Chem.* **2004**, *43*, 6383−6396.

(24) Onozawa-Komatsuzaki, N.; Kitao, O.; Yanagida, M.; Himeda, Y.; Sugihara, H.; Kasuga, K. *New J. Chem.* **2006**, *30*, 689−697.

(25) Nilsing, M.; Lunell, S.; Persson, P.; Ojamäe, L. *Surf. Sci.* **2005**, *582*, 49−60.

(26) Park, H.; Bae, E.; Lee, J. J.; Park, J.; Choi, W. *J. Phys. Chem. B* **2006**, *110*, 8740−8749.

(27) Nilsing, M.; Persson, P.; Ojamäe, L. *Chem. Phys. Lett.* **2005**, *415*, 375−380.

(28) Asbury, J. B.; Hao, E.; Wang, Y. Q.; Lian, T.; *J. Phys. Chem. B* **2000**, *104*, 11957−11964.

(29) Galoppini, E. *Coord. Chem. Rev.* **2004**, *248*, 1283−1207.

(30) Persson, P.; Lundqvist, M. J.; Ernstrofer, R.; Goddard, W. A., III; Willig, F. *J. Chem. Theory Comput.* **2006**, *2*, 441−451.

(31) Kilså, K.; Mayo, E. I.; Kuciauskas, D.; Villahermosa, R.; Lewis, N. S.; Winkler, J. R.; Gray, H. B. *J. Phys. Chem. A* **2003**, *107*, 3379−3383.

(32) Wang, D.; Mendelsohn, R.; Galoppini, E.; Hoertz, P. G.; Carlisle, R. A.; Meyer, G. J. *J. Phys. Chem. B* **2004**, *108*, 16642−16653.

(33) Persson, P.; Bergström, R.; Ojamäe, L.; Lunell, S. *Adv. Quantum Chem.* **2002**, *41*, 203−263.

(34) Persson, P.; Lunell, S.; Ojamäe, L. *Chem. Phys. Lett.* **2002**, *364*, 469−474.

(35) Persson, P.; Gebhardt, J. C. M.; Lunell, S. *J. Phys. Chem. B* **2003**, *107*, 3336−3339.

(36) Persson, P.; Lundqvist, M. J. In *Proceedings Volume of the Electrochemical Society: Electron Transfer in Nanomaterials*; Rumbles, G., Lian, T., Murakoshi, K., Eds.; Electrochemical Society: Pennington, NJ, 2006; PV2004−22, 27.

(37) Lundqvist, M. J.; Nilsing, M.; Persson, P.; Lunell, S. *Int. J. Quantum Chem.* **2006**, *106*, http://dx.doi.org/10.1102/qua.21088.

(38) Persson, P.; Bergström, R.; Lunell, S. *J. Phys. Chem. B* **2000**, *104*, 10384−10351.

(39) De Angelis, F.; Tilocca, A.; Selloni, A.; *J. Am. Chem. Soc.* **2004**, *126*, 15024−15015.

(40) Persson, P.; Lundqvist, M. J. *J. Phys. Chem. B* **2005**, *109*, 11918−11924.

(41) Meyer, G. J. *Inorg. Chem.* **2005**, *44*, 6852−6864.

(42) Willig, F.; Zimmermann, C.; Ramakrishna, S.; Storck, W. *Electrochim. Acta* **2000**, *45*, 4565−4575.

(43) Lanzafame, J. M.; Palese, S.; Wang, D.; Miller, R. J. D.; Muenter, A. A. *J. Phys. Chem.* **1994**, *98*, 11020−11033.

(44) Stier, W.; Duncan, W. R.; Prezhdo, O. V. *Adv. Mater.* **2004**, *16*, 240−244.

(45) Stier, W.; Prezhdo, O. V. *J. Phys. Chem. B* **2002**, *106*, 8047−8054.

(46) Rego, L. G. C.; Batista, V. S. *J. Am. Chem. Soc.* **2003**, *125*, 7989−7997.

(47) Wang, L. X.; May, V. *J. Chem. Phys.* **2004**, *121*, 8039−8049.

(48) Thoss, M.; Kondov, I.; Wang, H. B. *Chem. Phys.* **2004**, *304*, 169−181.

(49) Ramakrishna, S.; Willig, F.; May, V.; Knorr, A. *J. Phys. Chem. B* **2003**, *107*, 607−611.

(50) Frisch, M. J.; Trucks, G. W.; Schlegel, H. B.; Scuseria, G. E.; Robb, M. A.; Cheeseman, J. R.; Montgomery, J. A., Jr.; Vreven, T.; Kudin, K. N.; Burant, J. C.; Millam, J. M.; Iyengar, S. S.; Tomasi, J.; Barone, V.; Mennucci, B.; Cossi, M.; Scalmani, G.; Rega, N.; Petersson, G. A.; Nakatsuji, H.; Hada, M.; Ehara, M.; Toyota, K.; Fukuda, R.; Hasegawa, J.; Ishida, M.; Nakajima, T.; Honda, Y.; Kitao, O.; Nakai, H.; Klene, M.; Li,

X.; Knox, J. E.; Hratchian, H. P.; Cross, J. B.; Bakken, V.; Adamo, C.; Jaramillo, J.; Gomperts, R.; Stratmann, R. E.; Yazyev, O.; Austin, A. J.; Cammi, R.; Pomelli, C.; Ochterski, J. W.; Ayala, P. Y.; Morokuma, K.; Voth, G. A.; Salvador, P.; Dannenberg, J. J.; Zakrzewski, V. G.; Dapprich, S.; Daniels, A. D.; Strain, M. C.; Farkas, O.; Malick, D. K.; Rabuck, A. D.; Raghavachari, K.; Foresman, J. B.; Ortiz, J. V.; Cui, Q.; Baboul, A. G.; Clifford, S.; Cioslowski, J.; Stefanov, B. B.; Liu, G.; Liashenko, A.; Piskorz, P.; Komaromi, I.; Martin, R. L.; Fox, D. J.; Keith, T.; Al-Laham, M. A.; Peng, C. Y.; Nanayakkara, A.; Challacombe, M.; Gill, P. M. W.; Johnson, B.; Chen, W.; Wong, M. W.; Gonzalez, C.; Pople, J. A. *Gaussian 03*, revision B.05; Gaussian, Inc.: Wallingford, CT, 2003.

(51) Becke, A. D. *J. Chem. Phys.* **1993**, *98*, 5648−5652.

(52) Lee, C. T.; Yang, W. T.; Parr, R. G. *Phys. Rev. B* **1988**, *37*, 785−789.

(53) Dunning, T. H., Jr.; Hay, P. J. In *Modern Theoretical Chemistry*; Schefer, H. F., III., Ed.; Plenum: New York, 1976; Vol. 3, pp 1−28.

(54) Hay, P. J.; Wadt, W. R. *J. Chem. Phys.* **1985**, *82*, 299−310.

(55) Lashgari, K.; Kritikos, M.; Norrestam, R.; Norrby, T. *Acta Crystallogr., Sect. C1* **1999**, *55*, 64−67.

(56) Durand, P.; Barthelat, J. C. *Theor. Chim. Acta* **1975**, *38*, 283−302.

(57) Bouteiller, Y.; Mijoule, C.; Nizam, M.; Barthelat, J. C.; Daudey, J. P.; Pélissier, M.; Silvi, B. *Mol. Phys.* **1988**, *65*, 295−312.

(58) Hehre, W. J.; Radom, L.; Schleyer, P. V. R.; Pople, J. A. *Ab Initio Molecular Orbital Theory*; Wiley: New York, 1986.

(59) Persson, P.; Ojamäe, L. *Chem. Phys. Lett.* **2000**, *321*, 302−308.

(60) Gorelsky, S. I. *SWizard Program*; York University: Toronto, 1998; http://www.sg-chem.net/.

(61) Wyckoff, R. W. G. *Crystal Structures*, 2nd ed.; Interscience Publishers: New York, 1963; Vol. 1.

(62) Silvi, B.; Fourati, N.; Nada, R.; Catlow, C. R. A. *J. Phys. Chem. Solids* **1991**, *52*, 1005−1009.

(63) Fahmi, A.; Minot, C.; Silvi, B.; Causà, M. *Phys. Rev. B* **1993**, *47*, 11717−11724.

(64) Lunell, S.; Stashans, A.; Ojamäe, L.; Lindström, H.; Hagfeldt, A. *J. Am. Chem. Soc.* **1997**, *119*, 7374−7380.

(65) Muscat, J. P.; Newns, D. M. *Prog. Surf. Sci.* **1978**, *9*, 1−43.

(66) *MOLEKEL 4.3*; Flükiger, P., Lüthi, H. P., Portmann, S., Weber, J., Eds.; Swiss Center for Scientific Computing: Manno, Switzerland, 2000−2002. (b) Portmann, S.; Lüthi, H. P. *Chimia* **2000**, *54*, 766−770.

(67) *Grace-5.1.18*; http://plasma-gate.weizmann.ac.il/Grace/.

(68) Craig, D. C.; Scudder, M. L.; McHale, W. A.; Goodwin, H. A. *Aust. J. Chem.* **1998**, *51*, 1131−1139.

(69) Pyo, S.; Perez-Cordero, E.; Bott, S. G.; Echegoyen, L. *Inorg. Chem.* **1999**, *38*, 3337−3343.

(70) Ciofini, I.; Daul, C. A.; Adamo, C. *J. Phys. Chem. A* **2003**, *107*, 11182−11190.

(71) Zheng, K. C.; Wang, J. P.; Peng, W. L.; Liu, X. W.; Yun, F. C. *J. Mol. Struct. (THEOCHEM)* **2002**, *582*, 1−9.

(72) http://www.theochem.uni-stuttgart.de/pseudopotentiale/index.en.html.

(73) Andrae, D.; Haeussermann, U.; Dolg, M.; Stoll, H.; Preuss, H. *Theor. Chim. Acta* **1990**, *77*, 123−141.

(74) Martin, J. M. L.; Sundermann, A. *J. Chem. Phys.* **2001**, *114*, 3408−3420.

(75) Bergner, A.; Dolg, M.; Kuechle, W.; Stoll, H.; Preuss, H. *Mol. Phys.* **1993**, *80*, 1431−1441.

(76) Zakeeruddin, S. M.; Nazeeruddin, M. K.; Pechy, P.; Rotzinger, F. P.; Humphry-Baker, R.; Kalyanasundaram, K.; Grätzel, M.; Shklover, V.; Haibach, T. *Inorg. Chem.* **1997**, *36*, 5937−5946.

(77) Amouyal, E.; Mouallembahout, M.; Calzaferri, G. *J. Phys. Chem.* **1991**, *95*, 7641−7649.

(78) Sauvage, J. P.; Collin, J. P.; Chambron, J. C.; Guillerez, S.; Coudret, C.; Balzani, V.; Barigelletti, F.; Decola, L.; Flamigni, L. *Chem. Rev.* **1994**, *94*, 993−1019.

(79) Benkö, G.; Kallioinen, J.; Korppi-Tommola, J. E. I.; Yartsev, A. P.; Sundström, V. *J. Am. Chem. Soc.* **2002**, *124*, 489−493.

(80) Fantacci, S.; De Angelis, F.; Sgamellotti, A.; Re, N. *Chem. Phys. Lett.* **2004**, *396*, 43−48.

(81) Maestri, M.; Armaroli, N.; Balzani, V.; Constale, E. C.; Thompson, A. M. W. C. *Inorg. Chem.* **1995**, *34*, 2759−2767.

(82) Stone, M. L.; Crosby, G. A. *Chem. Phys. Lett.* **1981**, *79*, 169−173.

(83) Beltrán, A.; Sambrano, J. R.; Calatayud, M.; Sensato, F. R.; Andrés, J. *Surf. Sci.* **2001**, *490*, 116−124.

(84) Vittadini, A.; Selloni, A.; Rotzinger, F. P.; Grätzel, M. *Phys. Rev. Lett.* **1998**, *81*, 2954−2957.

(85) Redfern, P. C.; Zapol, P.; Curtiss, L. A.; Rajh, T.; Thurnauer, M. C. *J. Phys. Chem. B* **2003**, *107*, 11419−11427.

(86) McIntyre, N. S.; Thompson, K. R.; Weltner, W., Jr. *J. Phys. Chem.* **1971**, *75*, 3243−3249.

(87) Arlt, T.; Bermejo, M.; Blanco, M. A.; Gerward, L.; Jiang, J. Z.; Olsen, J. S.; Recio, J. M. *Phys. Rev. B* **2000**, *61*, 14414−14419.

(88) Tang, H.; Berger, H.; Schmid, P. E.; Lévy, F.; Burri, G. *Solid State Commun.* **1993**, *87,* 847−850.

(89) Kormann, C.; Bahnemann, D. W.; Hoffmann, M. R. *J. Phys. Chem.* **1988**, *92*, 5196−5201.

(90) Bae, E. Y.; Choi, W. Y.; Park, J. W.; Shin, H. S.; Kim, S. B.; Lee, J. S. *J. Phys. Chem. B* **2004**, *108*, 14093−14101.

(91) Gillaizeau-Gauthier, I.; Odobel, F.; Alebbi, M.; Argazzi, R.; Costa, E.; Bignozzi, C. A.; Qu, P.; Meyer, G. J. *Inorg. Chem.* **2001**, *40*, 6073−6079.

(92) Pechy, P.; Rotzinger, F. P.; Nazeeruddin, M. K.; Kohle, O.; Zakeeruddin, S. M.; Humphry-Baker, R.; Grätzel, M. *J. Chem. Soc. Chem. Commun.* **1995**, *1*, 65−66.

(93) Zabri, H.; Gillaizeau, I.; Bignozzi, C. A.; Caramori, S.; Charlot, M. F.; Cano-Boquera, J.; Odobel, F. *Inorg. Chem.* **2003**, *42*, 6655−6666.

(94) Zakeeruddin, S. M.; Nazeeruddin, M. K.; Pechy, P.; Rotzinger, F. P.; Humphry-Baker, R.; Kalyanasundaram, K.; Grätzel, M. *Inorg. Chem.* **1997**, *36*, 5937−5946.